

Early diagnosis of pancreatic ductal adenocarcinoma by signal-enhanced lateral flow immunoassay: SELFI

Received: 19 May 2025

Accepted: 24 January 2026

Published online: 05 February 2026

 Check for updates

Sohyeon Jang^{1,12}, Minsup Shin ^{1,12}, Jiseok Han ^{2,12}, Han-Joo Bae ¹, Yuna Youn³, Hye-Seong Cho¹, Kwanghee Yoo ¹, Jun-Sik Chu¹, Jaehyun An⁴, Geunhyeong An⁵, Hyejin Chang⁵, Jin-Hyeok Hwang^{3,6}, Jaehi Kim ¹✉, Jihwan Song ^{2,11}✉, Jong-chan Lee ^{3,6}✉, Luke P. Lee^{7,8,9,10}✉ & Bong-Hyun Jun ¹✉

Pancreatic ductal adenocarcinoma (PDAC) has a relatively low incidence but a high mortality rate, primarily due to difficulties in early detection. Current state-of-the-art methods for diagnosing early-stage PDAC tend to be invasive, time-consuming, and unreliable, primarily due to the difficulties associated with the early detection of pancreatic cancers. Here we show a quick and sensitive method for the early diagnosis of PDAC using a signal-enhanced lateral flow immunoassay called SELFI. We develop SELFI, which generates a strong colorimetric signal through multiple hotspots formed by plasmonic gold nanoparticles (AuNPs) assembled on a silica nanoparticle. Our SELFI assay achieves a 10,123-fold increase in the limit of detection compared to conventional lateral flow immunoassays using 20 nm AuNPs, providing results within 15 min. We demonstrate that SELFI enables early diagnosis of PDAC, as indicated by a receiver operating characteristic curve and a larger area under the curve compared to the enzyme-linked immunosorbent assay. SELFI's effective diagnostic features can enhance the timely identification of PDAC and may also serve in the early diagnosis of a range of other diseases.

Pancreatic ductal adenocarcinoma (PDAC) is one of the most lethal malignancies, with a 5-year survival rate of less than 10%, largely owing to challenges in early detection, aggressive tumor biology, and therapy resistance^{1–5}. Despite its clinical importance, early diagnosis of PDAC remains difficult because distinct symptoms are typically absent in the early stages, and the pancreas is difficult to examine using standard diagnostic methods due to its deep anatomical location^{5,6}. Although imaging modalities, such as computed tomography (CT), magnetic

resonance imaging, and endoscopic ultrasound are routinely used⁷, their invasiveness, high cost, and limited sensitivity for early-stage disease highlight the need for more accessible diagnostic tools.

As a noninvasive approach, diagnosing PDAC using biomarkers in biological samples, such as serum has been proposed. Numerous biomarkers for PDAC detection have been investigated; however, cancer antigen 19–9 (CA19–9) remains the only FDA-approved biomarker^{8–10} (Fig. 1a). CA19–9 has demonstrated reliability in

¹Department of Bioscience and Biotechnology, Konkuk University, Seoul, Republic of Korea. ²Department of Mechanical Engineering, Hanbat National University, Daejeon, Republic of Korea. ³Department of Internal Medicine, Seoul National University Bundang Hospital, Seongnam, Republic of Korea. ⁴Company of BioSquare, Hwaseong, Republic of Korea. ⁵Division of Science Education, Kangwon National University, Chuncheon, Republic of Korea. ⁶College of Medicine, Seoul National University, Seoul, Republic of Korea. ⁷Department of Medicine, Brigham and Women's Hospital, Harvard Medical School, Harvard University, Boston, MA, USA. ⁸Department of Bioengineering, University of California, Berkeley, CA, USA. ⁹Department of Electrical Engineering and Computer Science, University of California, Berkeley, CA, USA. ¹⁰Korea Biomedical Institute for Global Health Research and Technology (K-BIGHEART), Pohang University of Science and Technology (POSTECH), Pohang, Republic of Korea. ¹¹Present address: Department of Mechanical Engineering, Sogang University, Seoul, Republic of Korea. ¹²These authors contributed equally: Sohyeon Jang, Minsup Shin, Jiseok Han. ✉e-mail: susia45@gmail.com; jsong@sogang.ac.kr; ljc0316@snuh.org; lplee@harvard.edu; bjun@konkuk.ac.kr

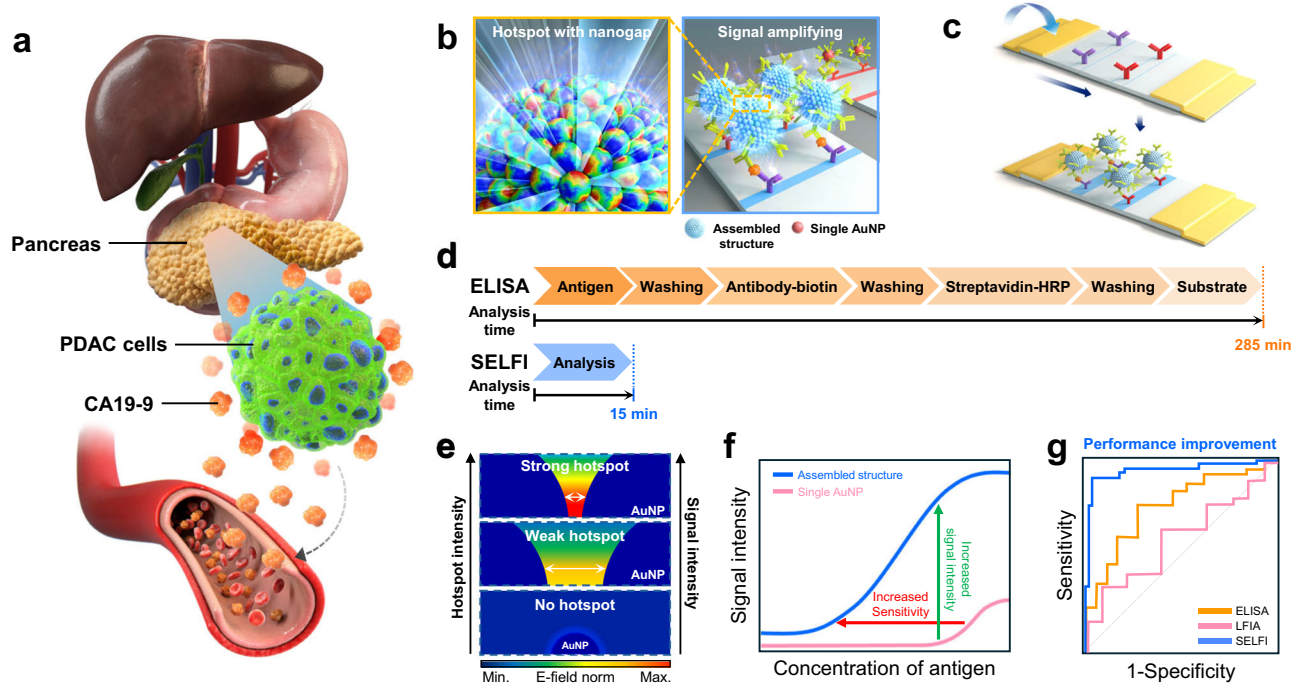


Fig. 1 | Quantification analysis of CA19-9 for early diagnosis of PDAC using the SELFI system. **a** Illustration of the pancreas and PDAC cells. PDAC cells are located in the pancreas, which is situated at a deep anatomical location. Overexpressed CA19-9 by PDAC cells is released into the bloodstream and elevates the CA19-9 level in serum samples. **b** Illustration of the assembled structure of the nanoprobe. Fabricated nanoprobe has multiple hotspots with nanogap that amplify the colorimetric signal. **c** Schematic illustration of the SELFI system for PDAC diagnosis. The colorimetric signal at the test line is generated by the binding of nanoprobe to the test line of the strip via interactions between CA19-9 and CA19-9 antibodies. **d** Comparison of the SELFI system with ELISA, one of the conventional methods for biomarker quantification analysis. The SELFI system required only 15 min for

analysis, whereas ELISA required 285 min. **e** Changes of E-field norm and colorimetric signal intensity of nanoprobe according to the gap distance between AuNPs. As the gap distance between AuNPs decreases, the E-field norm increases due to the generation of strong hotspots. **f** Model test for CA19-9 detection using LFIA, in which single 20 nm AuNPs were used as colorimetric nanoprobe, and SELFI. Compared with single AuNP-based LFIA, SELFI, which uses colorimetric nanoprobe with an assembled nanostructure, exhibited increased signal intensity and a wider dynamic range. **g** Schematic illustration of the ROC curve for PDAC diagnosis using ELISA (orange line), LFIA (red line), and SELFI (blue line). The gray dotted line represents a random classifier.

evaluating treatment responses in advanced PDAC; however, it has limitations as a screening marker for early-stage resectable PDAC when used with existing biomarker screening systems, such as enzyme-linked immunosorbent assay (ELISA)^{10,11}. To overcome the limitations of CA19-9, research efforts like CancerSEEK have aimed to discover new blood biomarkers beyond CA19-9^{12,13}. Despite these initiatives, the discovery of novel PDAC biomarkers presents challenges related to reproducibility and commercial viability. As an alternative, the development of a novel quantification system for CA19-9 to replace ELISA has been explored to enhance the sensitivity and efficacy of early PDAC diagnosis. For this purpose, PDAC diagnostic systems based on electrochemical immunosensors, photothermal immunoassay, or Raman spectroscopy have also been reported recently^{14–19}. However, even though exhibited quite low limit of detection (LOD), the developed diagnosis system still inconvenience to diagnosis because they required additional specialized instrument (such as electrochemical workstation^{14–16}, laser, thermometer¹⁷, or Raman spectrometer^{18,19}), and quite long analysis time (25–80 min).

As a solution to the inconvenience of such diagnostic systems, the lateral flow immunoassay (LFIA), which has been widely used for point-of-care testing because of its convenience, can be a candidate for PDAC diagnosis. The LFIA system is more user-friendly than conventional liquid biopsy methods, such as ELISA or electrochemical immunosensors, and the time necessary to obtain analysis results is very short (within 20 min)²⁰. Furthermore, compared to other methods, LFIA generally requires lower-cost instrumentation and simpler procedures, which could provide significant advantages in clinical practice. However, the colorimetric signal intensity of gold

nanoparticle (AuNP) probes, which are generally used as colorimetric nanoprobe, is sometimes insufficient to detect targets at low concentrations, necessitating the development of a new probe²¹.

Consequently, recent reports have demonstrated that not only silver nanoparticles (AgNPs) but also alloy-type metal NPs, such as Au/Ag, Au/Pt, and Au/Ir, and nanostructures, where NPs, such as AuNPs, alloy NPs, or quantum dots are assembled onto silica nanoparticles (SiO₂ NPs), can be used as probes for LFIA^{22–26}. The LOD with these developed probes is enhanced compared to AuNPs, and this advance has enabled the sensitive detection and quantification of various targets, such as exosomes²⁷, prostate cancer antigen (PSA)^{25,28}, hormones²⁹, carcinoembryonic antigen³⁰, and severe acute respiratory syndrome coronavirus 2^{26,31} using the LFIA system. Nevertheless, the quantitative analysis of CA19-9 using colorimetric signal-based LFIA for early PDAC diagnosis has rarely been reported, and in a few existing studies, the LOD was not adequate for highly sensitive analysis^{32,33}. Despite our recent report describing a colorimetric nanoprobe platform with enhanced sensitivity for LFIA, achieving an LOD of 0.04 U mL⁻¹ for CA19-9, the underlying mechanism responsible for the high sensitivity remains unclear, and quantitative analysis using clinical samples has not yet been performed³⁴.

In this study, we design a signal-enhanced lateral flow immunoassay (SELFI) system for the early diagnosis of PDAC through the quantitative analysis of CA19-9 in serum samples. SiO₂ NPs with assembled AuNPs (SiO₂@Au@Au NPs), which feature numerous hotspots due to nanogaps between the assembled AuNPs, are fabricated as the colorimetric nanoprobe in the SELFI system (Fig. 1b, c). Our SELFI system requires only 15 min after sample loading for the

quantitative analysis of CA19-9 in serum samples, while the commonly used ELISA for biomarker quantification requires over 4 h and involves a complex experimental process (Fig. 1d). The colorimetric signal intensity of SELFI is significantly higher than that of conventional LFIA at the same CA19-9 concentration, thanks to the hotspots in $\text{SiO}_2@\text{Au}$ NPs, which markedly enhance colorimetric signal intensity (Fig. 1e). The LOD of CA19-9 in SELFI is 10,123-fold lower than that of conventional LFIA (Fig. 1f). As a diagnostic system for PDAC based on the quantitative analysis of CA19-9, SELFI exhibits superior diagnostic performance compared to both ELISA and conventional LFIA, as indicated by their receiver operating characteristic (ROC) curves and area under the curve (AUC) values. Notably, SELFI demonstrates significant improvement in the early diagnosis of PDAC (Fig. 1g).

Results

Design of colorimetric nanoprobe for SELFI using numerical simulation

Reportedly, hotspots induced by plasmonic coupling at the nanogaps between metal NPs, including AuNPs and Au/Ag NPs, exhibit unique optical characteristics, such as enhanced electric fields, absorption, and scattering³⁵. Utilizing these properties, various plasmonic nanostructures, such as metal NP-decorated structures, Au multimer assemblies, and metal NP 3D clusters, have been developed for applications in SERS^{36–38}, photocatalytic hydrogen production^{39–41}, and colorimetric biosensing and imaging^{42–45}. In particular, assembling metal NPs on the surface of core NPs, including Au/Ag hollow-shell-assembled silica nanospheres for SERS⁴⁶ and plasmonic microgels for temperature monitoring⁴⁷ is an effective strategy for generating and harnessing plasmonic hotspots. Based on previous studies, we adopted this approach in designing our plasmonic nanostructures (Fig. 2a). Previous simulation studies on assembled nanoparticle structures have investigated electric field enhancement using simplified geometries⁴⁸, optical characteristics using fully three-dimensional geometries⁴⁹, and LSPR wavelength tuning based on gap-to-diameter ratios⁵⁰. However, the relationship between hotspot-enhanced electric field intensity, which directly affects the colorimetric signal, and key parameters, such as the gap distance between AuNPs (G_{Au}) and the diameter of AuNPs (D_{Au}) has not yet been comprehensively investigated from a fully 3D structural perspective. Numerical simulations were performed to investigate the relationships between the optical properties of AuNPs-assembled silica NPs and these parameters, particularly G_{Au} and D_{Au} , to aid in the *in silico* design of innovative colorimetric nanoprobe for SELFI.

Supplementary Fig. 1 illustrates a schematic of the 3D model geometry and the various cases considered in the simulation. The assembled nanostructure comprised SiO_2 NPs with a diameter of 168 nm, and 270 AuNPs were evenly distributed on its surface. The electric field was oriented in the y-direction. Six simulation cases were analyzed, with G_{Au} values of 10, 8, 6, 4, 2, and 1 nm. Since the diameter of the SiO_2 NP and the count of AuNPs were fixed, D_{Au} increased as G_{Au} decreased. Using these designed assembled nanostructures, a wave-optics simulation was performed in the visible wavelength range, assuming that the assembled nanostructures were immersed in water.

Based on the simulation results, the electric field norm spectra of each model in the visible wavelength range were analyzed (Supplementary Fig. 2a). The electric field on the surface of the assembled nanostructure became stronger as G_{Au} decreased, and hotspots emerged between the AuNPs when G_{Au} was less than 6 nm (Fig. 2b). The results indicated that the overall intensity of the electric field increased with decreasing G_{Au} , with a particularly notable increase at the peak wavelength. In addition, according to the simulation results, the particle properties associated with the electric field, including absorption, scattering, and extinction cross-sections, were enhanced

as the electric field intensity increased (Fig. 2c and Supplementary Fig. 2b, c).

Although the absorption cross-section increased as G_{Au} decreased, it remained unclear whether this increase was attributed to the reduction in G_{Au} or the rise in D_{Au} , as both parameters changed simultaneously. To determine which parameter had a more significant impact on increasing the absorption cross-section of the nanostructure, the change in the absorption cross-section of a single AuNP on the assembled nanostructure was compared with that of a single AuNP on a SiO_2 substrate (Supplementary Figs. 3 and 4; Fig. 2d, e). As shown in Supplementary Fig. 4, the electric field of a single AuNP on the SiO_2 substrate increased as D_{Au} increased. In contrast, the electric field from the AuNPs on the assembled nanostructure increased dramatically with the creation of hotspots between the AuNPs when G_{Au} was reduced to a certain distance (Fig. 2d). Because of this phenomenon, the absorption cross-section of AuNPs within the assembled nanostructure was nearly 2.65-fold higher than that of a single AuNP on a SiO_2 substrate at the largest D_{Au} , despite being nearly identical at the smallest D_{Au} (Fig. 2e). In addition, we confirmed that decreasing G_{Au} while keeping D_{Au} constant induced a more pronounced change in hotspot formation than increasing D_{Au} with a fixed G_{Au} (Supplementary Fig. 5). This comparison suggests that G_{Au} , which is closely linked to the generation of hotspots between AuNPs, plays a more significant role than D_{Au} in enhancing the electric field, leading to an increased absorption cross section. This absorption enhancement could directly contribute to the colorimetric signal intensity of the SELFI system.

We confirmed that the assembled nanostructure exhibited a significantly higher absorption intensity than a single 20 nm AuNP, which is the gold standard nanoprobe for conventional LFIA (Supplementary Fig. 6). These simulation results suggest that the amplification of the electric field around the assembled nanostructure, resulting in a strong absorption intensity, is not solely due to the increase in D_{Au} but is mainly driven by the formation of hotspots caused by the decrease in G_{Au} as D_{Au} increases.

Based on these simulation results, we could expect that our designed $\text{SiO}_2@\text{Au}@Au$ NPs should exhibit a more intense colorimetric signal due to the electric field enhancement effect caused by hotspots formed between AuNPs with under the specific distance. This enhancement renders them superior to single AuNPs, which are commonly used as nanoprobe in conventional LFIA system.

Fabrication and characterization of nanoprobe

Based on the simulation results, we fabricated $\text{SiO}_2@\text{Au}@Au$ NPs via a seed-mediated growth method, with controlling the nanogaps as colorimetric nanoprobe for SELFI (Fig. 2f and Supplementary Fig. 7). As shown in Supplementary Fig. 8, AuNP growth on the surface of aminated SiO_2 NPs was systematically controlled by varying the amounts of Au precursor and ascorbic acid. The resulting nanostructures were denoted as $\text{SiO}_2@\text{Au}@Au_1$ to $\text{SiO}_2@\text{Au}@Au_{11}$ according to the reagents used.

Figure 2g shows the Cs-corrected scanning transmission electron microscopy (Cs-STEM) images of $\text{SiO}_2@\text{Au}@Au_1$, $\text{SiO}_2@\text{Au}@Au_3$, $\text{SiO}_2@\text{Au}@Au_5$, $\text{SiO}_2@\text{Au}@Au_7$, $\text{SiO}_2@\text{Au}@Au_9$, and $\text{SiO}_2@\text{Au}@Au_{11}$. The average G_{Au} for each nanostructure was 9.55, 7.63, 5.89, 3.53, 1.33, and 1.20 nm, respectively. This decrease in G_{Au} resulted from the increase in D_{Au} , which was based on the amount of Au^{3+} precursor used during the fabrication process (Supplementary Fig. 9).

After fabricating $\text{SiO}_2@\text{Au}@Au$ NPs, the optical properties of each nanoprobe were characterized to select the optimal colorimetric nanoprobe for SELFI. First, the degree of visible light extinction, strongly related to the colorimetric signal intensity of the SELFI system, was measured. As shown in Fig. 2h, the extinction of visible light by the $\text{SiO}_2@\text{Au}@Au$ NPs increased as the G_{Au} of $\text{SiO}_2@\text{Au}@Au$ NPs was decreased, following the same trend observed in the numerical simulation. Based on these extinction spectra, the color of the

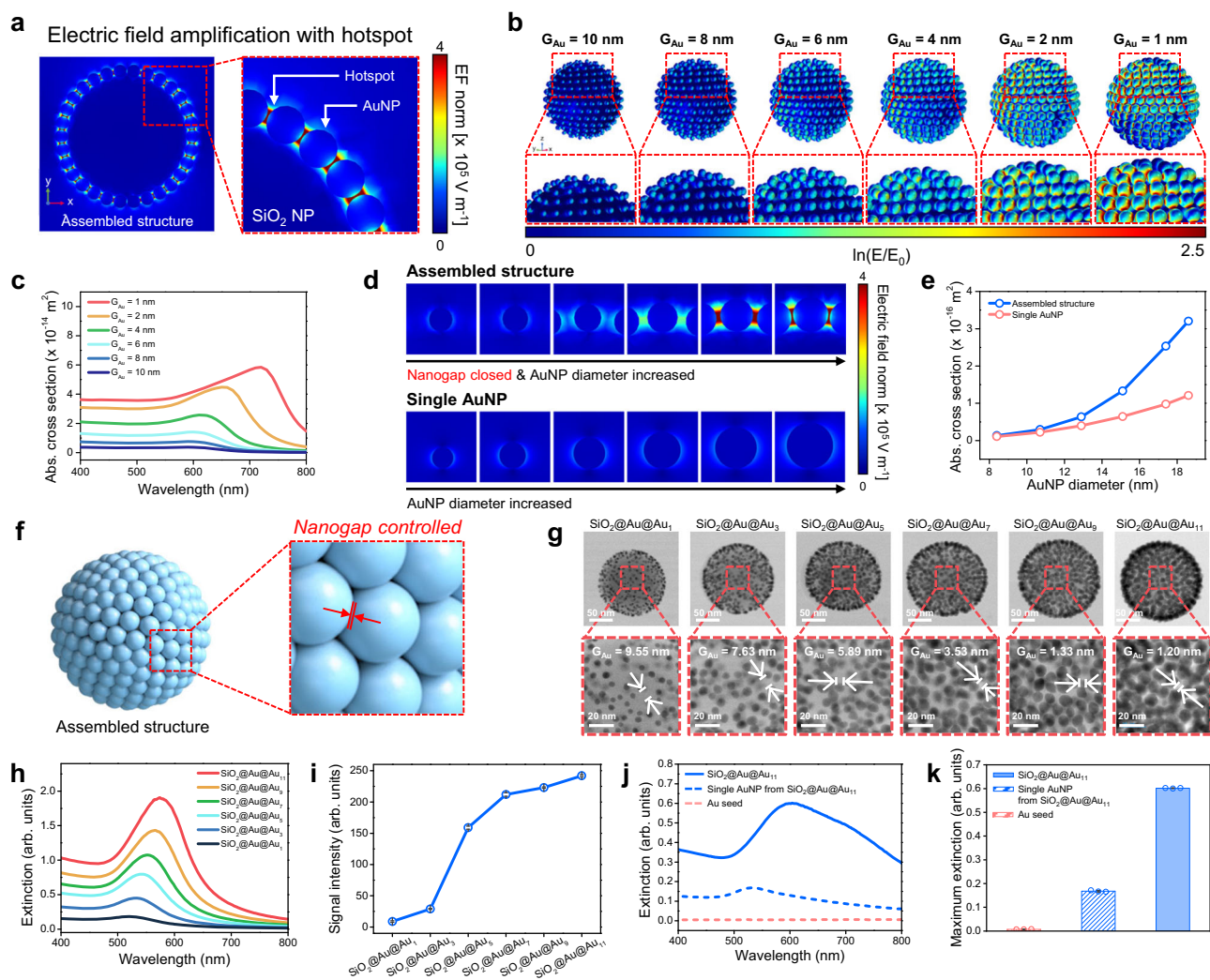


Fig. 2 | Design with numerical simulation, fabrication, and characterization of colorimetric nanoprobes for SELFI. **a** Maximum electric field amplification of the assembled nanostructure induced by hotspots between AuNPs on SiO_2 NP. **b** Electric field distribution at peak wavelength depending on G_{Au} . **c** Absorption cross-section spectra depending on G_{Au} . **d** Comparison of electric field norm distribution (at each peak wavelength) between a single AuNP and an AuNP on the assembled nanostructure, depending on AuNP diameter. **e** Absorption cross-section intensity of a single AuNP (red line) and an AuNP on the assembled nanostructure (blue line) at peak wavelength, depending on AuNP diameter. **f** Schematic illustration of fabricated nanoprobes with an assembled nanostructure. AuNPs were located onto the surface of SiO_2 nanotemplates with controlled nanogaps. **g** Cs-STEM images of fabricated $\text{SiO}_2@Au@Au_1$, $\text{SiO}_2@Au@Au_3$, $\text{SiO}_2@Au@Au_5$, $\text{SiO}_2@Au@Au_7$, $\text{SiO}_2@Au@Au_9$, and $\text{SiO}_2@Au@Au_{11}$. The average gap distances between AuNPs were 9.55, 7.63, 5.89, 3.53, 1.33, and 1.20 nm, respectively.

G_{Au} was measured from 20 individual AuNP–AuNP gap measurements per condition, obtained from a representative Cs-STEM image ($n = 20$ individual measurements). Scale bars, 50 nm (upper images) and 20 nm (lower images). **h** UV–vis extinction spectra of fabricated NPs. **i** Colorimetric signal intensity of fabricated NPs on NC membrane. The colorimetric signal intensity was measured using the ImageJ software. Quantitative data represent mean \pm SD from three independent experiments, each performed using separately prepared batches from the same sample ($n = 3$). **j** UV–vis extinction spectra of $\text{SiO}_2@Au@Au_{11}$ (blue solid line), AuNPs from $\text{SiO}_2@Au@Au_{11}$ (blue dotted line), and 3–5 nm AuNPs (red dotted line). **k** Extinction at $\lambda_{\text{max,ext}}$ of $\text{SiO}_2@Au@Au_{11}$ (blue filled bar), AuNPs from $\text{SiO}_2@Au@Au_{11}$ (blue hatched bar), and 3–5 nm AuNPs (red hatched bar). Bars represent mean \pm SD, with individual data points shown as jittered dots from three independent experiments, each performed using separately prepared batches from the same sample ($n = 3$).

$\text{SiO}_2@Au@Au$ NP mixture deepened as the G_{Au} of $\text{SiO}_2@Au@Au$ NPs was decreased (Supplementary Fig. 10). Similarly, the intensity of the colorimetric signals from the $\text{SiO}_2@Au@Au$ NPs on the nitrocellulose (NC) membrane exhibited the same trend, with the colorimetric signal intensity from $\text{SiO}_2@Au@Au_{11}$ NPs nearly reaching the maximum measurable value (Fig. 2i).

To identify the experimental primary factor behind this increase, the extinction spectra of Au nanoseeds (3–5 nm), $\text{SiO}_2@Au@Au_{11}$ NPs, and AuNPs obtained from $\text{SiO}_2@Au@Au_{11}$ NPs after removing the SiO_2 nanotemplate were measured (Fig. 2j). The effect of AuNP diameter was evaluated by comparing the extinction of Au nanoseeds with that of single AuNPs from $\text{SiO}_2@Au@Au_{11}$ NPs, which could be regarded as individual AuNPs with large interparticle distances. The effect of gap

distance was assessed by comparing $\text{SiO}_2@Au@Au_{11}$ NPs with AuNPs from $\text{SiO}_2@Au@Au_{11}$ NPs, as the AuNP diameter remained unchanged after SiO_2 nanotemplate removal.

A comparison of the maximum extinction of each nanostructure at their maximum extinction wavelength ($\lambda_{\text{max,ext}}$) showed that the degree of extinction increased slightly from 0.031 (Au nanoseeds) to 0.120 (single AuNPs from $\text{SiO}_2@Au@Au_{11}$ NPs) due to the increase in AuNP diameter. However, the extinction increased significantly to 0.426 for $\text{SiO}_2@Au@Au_{11}$ NPs, attributed to the localized surface plasmon resonance effect of the nanogaps between the AuNPs (Fig. 2k). These results experimentally confirm that the extinction of visible light by the fabricated nanostructure is more influenced by the gap distance between AuNPs than by AuNP diameter.

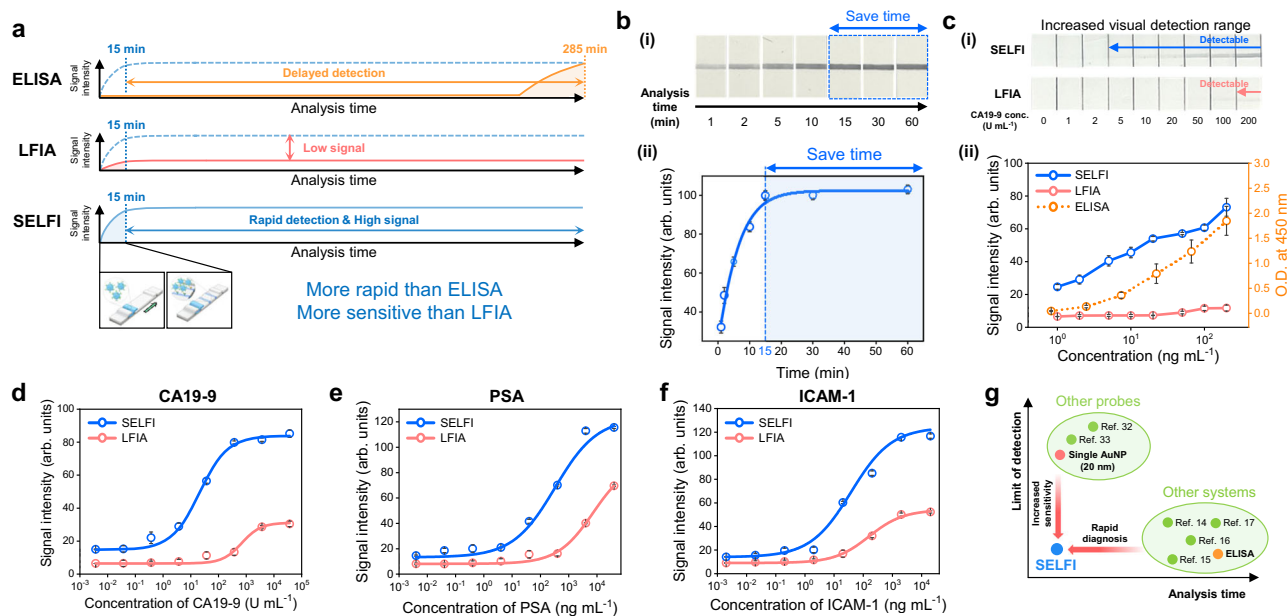


Fig. 3 | Model test for quantification of CA19-9 using SELFI. **a** Schematic illustration of time-dependent signal intensity from ELISA, conventional LFIA, and SELFI during biomarker quantification analysis. **b–i** Photographs of the NC membrane after CA19-9 quantification analysis depending on the analysis time. **ii** Signal intensity graph as a function of analysis time. The concentration of CA19-9 in the analyte sample was 3700 U mL^{-1} , and the calibration curve was fitted using the Boltzmann model. **c–i** Photographs of the NC membrane after developing the CA19-9 solution with SELFI and LFIA, depending on the concentration of CA19-9. **ii** Signal intensity graph as a function of CA19-9 concentration. The blue line, red line, and orange dotted line represent signals from SELFI, LFIA, and ELISA, respectively. The gray

dotted line represents the boundary for naked-eye detection in SELFI and LFIA. **d** Calibration curve for CA19-9 quantification. **e** Calibration curve for PSA quantification. **f** Calibration curve for ICAM-1 quantification. **g** Comparison of SELFI for PDAC diagnosis with other LFIA-based diagnostic systems and other diagnostic systems, including ELISA. For **b–f**, the colorimetric signal intensity was measured using the ImageJ software. For **d–f**, the blue line and circles represent the results using SELFI, while the red line and circles represent the results using LFIA. For **d–f**, the calibration curves were fitted using sigmoidal curves. Quantitative data represent mean \pm SD from three independent experiments, each performed using separately prepared batches from the same sample ($n = 3$). Representative images are shown.

To verify the superior optical properties of $\text{SiO}_2@\text{Au}@\text{Au}_{11}$ NPs as colorimetric nanoprobes, they were compared with 20 nm AuNPs for conventional LFIA, and 200 nm AuNPs, which are similar in diameter to $\text{SiO}_2@\text{Au}@\text{Au}_{11}$ NPs. In terms of visible light extinction, the maximum extinction value of $\text{SiO}_2@\text{Au}@\text{Au}_{11}$ NPs was 58-fold higher than that of 200 nm AuNPs and 1439-fold higher than that of 20 nm AuNPs (Supplementary Fig. 11). As shown in Supplementary Fig. 12, representative dark-field microscopy images are provided to qualitatively illustrate the plasmonic scattering characteristics of the nanoprobes. Only $\text{SiO}_2@\text{Au}@\text{Au}_{11}$ NPs appeared brightly, whereas the other nanoprobes showed weak scattering.

Finally, the colorimetric signal intensity of $\text{SiO}_2@\text{Au}@\text{Au}_{11}$ NPs on the NC membrane was significantly higher than that of 20 nm AuNPs on the NC membrane when the particle concentration exceeded a certain level (Supplementary Fig. 13). In summary, our fabricated $\text{SiO}_2@\text{Au}@\text{Au}_{11}$ NPs exhibited superior optical properties as colorimetric nanoprobes compared to conventional AuNPs.

Quantification of CA19-9 using SELFI

After fabricating and characterizing $\text{SiO}_2@\text{Au}@\text{Au}$ NPs, a model test was conducted for the quantitative analysis of CA19-9 using the SELFI system, which has the potential to be faster than ELISA and more sensitive than LFIA (Fig. 3a). First, the change in colorimetric signal over time was examined to determine the optimal analysis time for SELFI. As shown in Fig. 3b, the intensity of the test line's colorimetric signal increased with time, with no further significant changes observable by the naked eye after 15 min. This trend was further confirmed by quantifying the colorimetric signal intensity using ImageJ, which demonstrated that the intensity saturated after 15 min. These results indicate that quantification of CA19-9 in the sample using SELFI can be completed in just 15 min—significantly shorter than the 285 min required for ELISA.

Next, the colorimetric signals obtained from the SELFI, LFIA, and ELISA systems at various CA19-9 concentrations ($0\text{--}200 \text{ U mL}^{-1}$) were compared (Fig. 3c). In the SELFI system, represented by a navy-colored line as a signal, the colorimetric signal of test line signal was detectable by the naked eye when the CA19-9 concentration exceeded 5 U mL^{-1} . However, no visible signals were detected in the LFIA system until the CA19-9 concentration reached 100 U mL^{-1} , and even at this concentration, only a faint red line was observed. These tendencies were further confirmed by quantifying the colorimetric signal intensity using the ImageJ software. For the SELFI system, the signal intensity was 24.67 at a CA19-9 concentration of 1 U mL^{-1} and reached 73.17 at 200 U mL^{-1} . This increase was significantly greater than that observed in the LFIA system employing single AuNPs, where the signal intensity changed from 6.59 to 11.76, over the same CA19-9 concentration range. Considering that ELISA, a well-established high-sensitivity detection method for target biomarkers, exhibited a similar signal increase pattern, these results suggest that the SELFI system offers a level of sensitivity comparable to that of ELISA for the detection of target biomarkers, including CA19-9.

After verifying the fundamental characteristics of the SELFI system, calibration curves were obtained for the quantification of CA19-9 using each nanoprobe and corresponding standard solutions. The colorimetric signals from the test lines of both nanoprobes were measured using the ImageJ software, and the calibration curve of each analysis method was determined through sigmoidal fitting (Fig. 3d and Supplementary Fig. 14). The equation for the calibration curve of the SELFI is as follows:

$$\text{Signal intensity} = 83.84 + \frac{(14.75 - 83.84)}{1 + \left(\frac{\text{Concentration}}{20.62}\right)^{0.85}} \quad (1)$$

For single AuNP-based LFIA, the calibration curve was:

$$\text{Signal intensity} = 31.13 + \frac{(6.45 - 31.13)}{1 + \left(\frac{\text{Concentration}}{689.82}\right)^{1.26}} \quad (2)$$

The LOD of each system was calculated based on calibration curves (Supplementary Table 1). The LOD for CA19-9 using SELFI was 0.012 U mL⁻¹, which was more than 10,123-fold lower than that of a single AuNP-based LFIA (121.477 U mL⁻¹) and 25-fold lower than that of commercially available ELISA (0.3 U mL⁻¹). Furthermore, the LOD of SELFI was lower than that of previously reported LFIA systems for CA19-9 quantification³³, indicating that SELFI is among the most sensitive LFIA systems for CA19-9 detection. Similar trends were observed not only for CA19-9 but also for PSA and intercellular adhesion molecule 1 (ICAM-1), which are frequently used as cancer biomarkers. Therefore, the SELFI system could serve as a substitute for conventional LFIA systems, regardless of the target biomarker type (Fig. 3e, f).

To further assess the performance of SELFI as a diagnostic system, CA19-9 quantification-based PDAC diagnostic methods reported in the literature and those that are commercially available were compared by plotting analysis time versus LOD (Fig. 3g). The results demonstrated that SELFI quantification of CA19-9 required a short analysis time, comparable to conventional LFIA⁵¹, LFIA with carbon nanotubes³², and time-resolved fluorescence microsphere-based LFIA³³, all of which have relatively high LODs. Conversely, SELFI exhibited a lower LOD than or similar to that of commercially available ELISA kits, electrochemical immunosensors^{14–16}, and near-infrared photothermal immunoassays¹⁷, which require longer analysis time. These results highlight that SELFI effectively combines the advantages of previously published diagnostic platforms and commercially available assays, providing both rapid analysis and a low LOD.

Diagnosis of PDAC via CA19-9 quantification in serum samples using SELFI

Using LFIA and the designed SELFI system, quantification of CA19-9 in serum samples from healthy controls (50 ea.), patients in early-stage PDAC (40 ea.), and patients in late-stage PDAC (60 ea.) was conducted to determine the possibility of early diagnosis of PDAC using the SELFI system. After taking photographs of the test strips, the concentration of CA19-9 in each serum sample was successfully calculated by measuring the colorimetric signal intensity of the test lines using the ImageJ software (Supplementary Figs. 15;16 and Supplementary Dataset 1). To compare the diagnostic performance of SELFI with that of ELISA, which is commonly used for the quantification of CA19-9, and LFIA, the ROC curve and AUC values of each system were compared. The ROC curve and AUC value were calculated after 90% of the samples were extracted from the mother populations, and this process was repeated 100 times to enhance statistical reliability (Fig. 4a).

Figure 4b–d shows the average ROC curves of each system, in which the mother population was set as samples from healthy controls and early-stage patients (Fig. 4b), healthy controls and late-stage patients (Fig. 4c), and total samples (Fig. 4d). The average AUC value of SELFI was significantly higher than that of ELISA for samples from healthy controls and early-stage patients (0.862 and 0.854, respectively), indicating that our SELFI system performed notably better for the early diagnosis of PDAC than ELISA. The AUC values of both diagnostic systems were almost the same for samples from healthy controls and late-stage patients (0.925 for SELFI and 0.926 for ELISA, respectively). For the total serum samples, the AUC value of SELFI was slightly higher than that of ELISA (0.899 for SELFI and 0.896 for ELISA, respectively). Finally, LFIA, which used 20 nm AuNPs as colorimetric nanoprobe, showed poor AUC values in all cases compared to the other two systems (0.550 for healthy controls and early-stage patients, 0.692 for healthy controls and late-stage patients, and 0.634 for total samples). The calculated AUC values for all repetition steps were

plotted as violin plots to confirm the statistical evaluation of the differences in AUC values among ELISA, LFIA, and SELFI (Fig. 4e–g). The *P* values for the comparison between ELISA and SELFI were <0.0001, 0.0142, and 0.3363 for healthy controls versus early stage PDAC, whole PDAC, and late-stage PDAC, respectively (Table 1). For the comparison between LFIA with single AuNPs and the other systems, all *P* values were <0.0001. Based on these results, the superior performance of the SELFI system for PDAC diagnosis, particularly for early diagnosis, was statistically proven.

Discussion

We designed and fabricated SiO₂@Au@Au NPs, where AuNPs were embedded on the surface of SiO₂ NPs, as colorimetric nanoprobe for the LFIA system for the early diagnosis of PDAC. To the best of our knowledge, this study reports simulations of the electric field with controlled gap distances between AuNPs on SiO₂ NPs and the application of AuNP-embedded SiO₂ NPs as colorimetric nanoprobe in an LFIA system for the early diagnosis of PDAC.

Our fabricated nanoparticle consisted of SiO₂ NP and AuNPs, where the AuNPs were located on the surface of the SiO₂ NP with nanogaps. The SiO₂ NP core was chosen because it can be fabricated easily with a controlled size using Stöber or its modified methods^{52,53}, and the surface of SiO₂ NP can be modified with silane derivatives, such as (3-aminopropyl)triethoxysilane (APTES)⁵⁴. Furthermore, the SiO₂ core does not interfere with the growth of AuNPs during the seed-mediated growth process, and the size and gap distance between the grown AuNPs can be well controlled. Consequently, the reproducibility of the morphology of SiO₂@Au@Au₁₁ NP was ensured. This advantage was particularly evident when compared to Au-Au core/satellite structures, in which AuNPs were located on the surface of the AuNP core with an uncontrolled gap distance⁵⁵.

The relationship between the colorimetric signal intensity in LFIA and electric field enhancement from plasmonic behavior can be described by the following mechanism: increasing the electric field by the plasmonic hotspot effect leads to an increase in the absorption cross-section, which is proportional to the square of the local electric field. As the absorption cross-section increases, a smaller portion of the incident light was reflected owing to the increasing absorption ratio of the incident light by the NPs. As a result, NPs with high absorption cross-sections appear darker in color owing to the lack of reflected incident light, and this dark color exhibits high colorimetric signal intensity because of its high contrast with the white color, which is the color of the NC membrane. With this mechanism, the SiO₂@Au@Au₁₁ NPs demonstrated more intense colorimetric signals than commercially used single AuNPs of 20 nm, owing to the presence of abundant hotspots between the embedded AuNPs.

With this optical characteristic, our SELFI system has several merits compared to other diagnostic systems, such as ELISA or LFIA with single AuNPs. First, the quantification of CA19-9 using the SELFI system was performed within 15 min, whereas ELISA required more than 4 h for quantification. Second, the LOD of SELFI was 0.012 U mL⁻¹, which was 10,123-fold and 25-fold lower than that of single AuNPs (124.77 U mL⁻¹) and commercially available ELISA kit (0.3 U mL⁻¹), respectively. Finally, the AUC value of the ROC curve from SELFI was higher than that from ELISA (0.862 vs. 0.854, *P* < 0.0001 in healthy controls versus early stage PDAC, and 0.896 vs. 0.899, *P* = 0.0142 in healthy controls versus whole PDAC). This indicates that SELFI is a more effective diagnostic system for the early diagnosis of PDAC than conventional ELISA.

Encouraged by the potential of the SELFI system as a disease diagnostic platform, we aim to further improve its reliability and convenience through the following future efforts. First, we will optimize the fabrication conditions for SiO₂@Au@Au₁₁ with high reproducibility using a fully assembled kit, including conjugate and sample pads. Second, we will establish a standardized method for analyzing

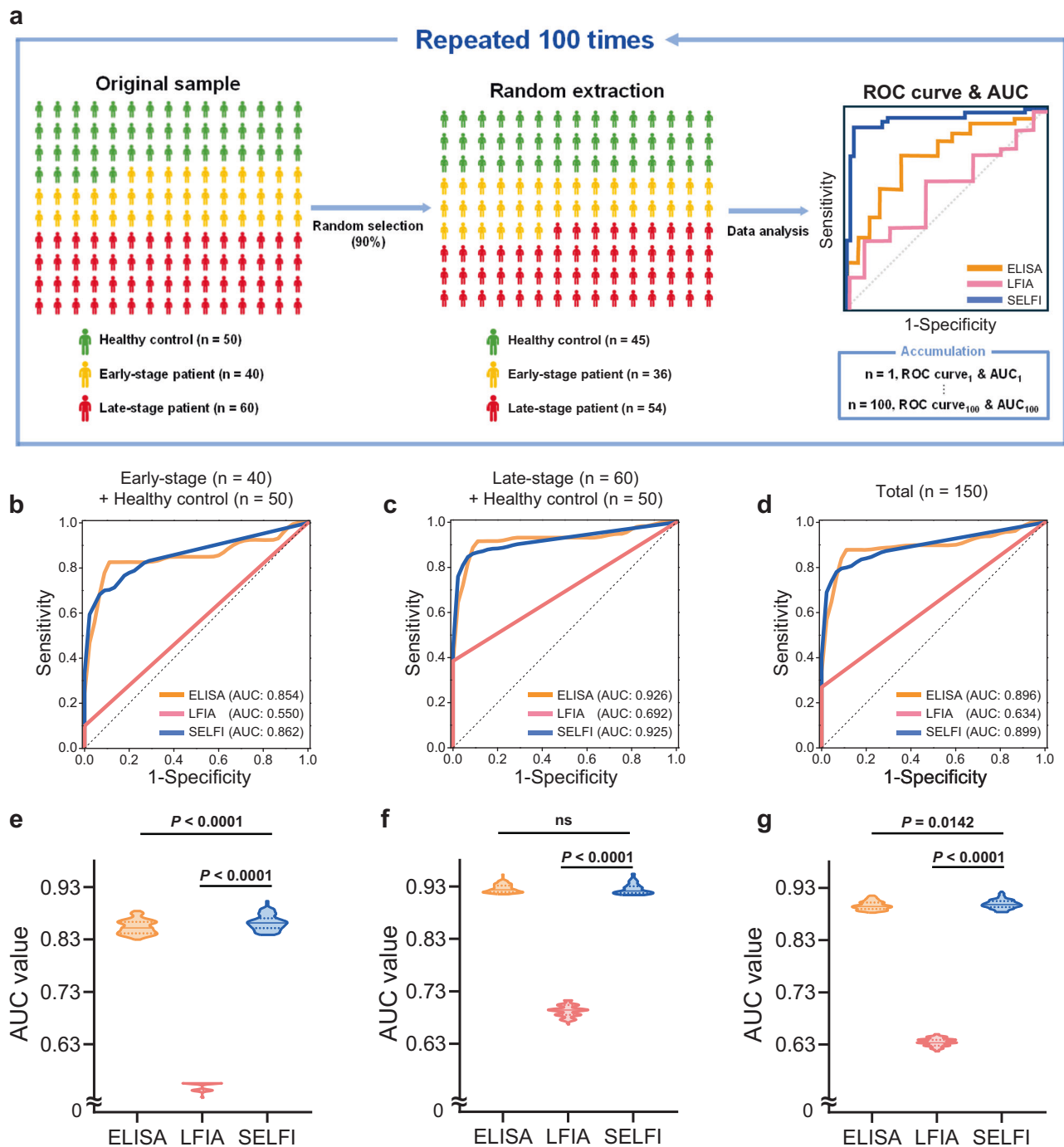


Fig. 4 | Diagnosis of PDAC with clinical serum samples using ELISA, LFIA, and SELFI. **a** Schematic illustration of the statistical data analysis process.

b Average ROC curve for ELISA, LFIA, and SELFI using samples from early-stage PDAC patients and healthy controls (area under the curve (AUC): ELISA = 0.854, LFIA = 0.550 and SELFI = 0.862). **c** Average ROC curve for ELISA, LFIA, and SELFI using samples from late-stage PDAC patients and healthy controls (AUC: ELISA = 0.926, LFIA = 0.692 and SELFI = 0.925). **d** Average ROC curve for ELISA, LFIA, and SELFI using total samples (AUC: ELISA = 0.896, LFIA = 0.634 and SELFI = 0.899). **e** Violin plot of AUC values for ELISA, LFIA, and SELFI using samples from early-stage PDAC patients and healthy controls ($P < 0.0001$, two-sided Student's t test). **f** Violin plot of AUC values for ELISA, LFIA, and SELFI using samples from late-stage PDAC

patients and healthy controls. Two-sided Student's t test shows a significant difference between LFIA and SELFI ($P < 0.0001$), but not between ELISA and SELFI (ns; $P = 0.3363$). **g** Violin plot of AUC values for ELISA, LFIA, and SELFI using total samples. Statistical significance was assessed using a two-sided Student's t test (ELISA vs. SELFI, $P = 0.0142$; LFIA vs. SELFI, $P < 0.0001$). For **b–g**, data from ELISA, LFIA, and SELFI are depicted in orange, red, and blue, respectively. The ROC curves and AUC values were obtained using a homemade R program code with the pROC library. For **b–d**, the average ROC curves were obtained by averaging 100 ROC curves using linear interpolation, with the black dotted line representing a random classifier. For **e–g**, the median value is depicted as a solid line, and the interquartile range boundaries are depicted as dotted lines in each violin plot.

colorimetric signals. Third, we will determine an optimal cutoff for PDAC diagnosis using the SELFI system by applying machine-learning algorithms to the data analysis framework. Fourth, samples will be collected from additional independent cohorts with diverse ethnic and

geographic backgrounds to further enhance statistical robustness and generalizability, as guided by the post-hoc power analysis of the current dataset (Supplementary Table 3). Fifth, we will seek to reduce potential misclassification in Lewis-negative cases⁵⁶ by integrating

Table 1 | AUC calculations for ELISA, LFIA, and SELFI results at 95% CIs (100 repetitions)

Samples	Diagnosis system					
	ELISA		LFIA		SELFI	
	AUC	95% CI	AUC	95% CI	AUC	95% CI
Early-stage (<i>n</i> = 40) + healthy control (<i>n</i> = 50)	0.854	0.834–0.881	0.550	0.528–0.556	0.862	0.841–0.888
Late-stage (<i>n</i> = 60) + healthy control (<i>n</i> = 50)	0.926	0.917–0.940	0.692	0.676–0.713	0.925	0.914–0.949
Early-stage (<i>n</i> = 40) + late-stage (<i>n</i> = 60) + healthy control (<i>n</i> = 50)	0.896	0.885–0.913	0.634	0.619–0.647	0.899	0.884–0.919

quantitative information from additional biomarkers with CA19-9. Finally, we will extend the application of the SELFI system to other biomarkers to enable the diagnosis of additional critical diseases for which early detection is essential. With these efforts, the SELFI system may provide improved convenience, sensitivity, and reliability, and could offer an alternative approach for the early diagnosis of PDAC, with potential applications in preventive healthcare.

Method

Ethics statement

Ethical approval was obtained from the Human Bioresource Center of Seoul National University Bundang Hospital (Affiliated College of Medicine, Seoul National University). The study protocol was reviewed and approved by the Institutional Review Board (IRB approval number: X-2011-651-903) and conducted in accordance with the Declaration of Helsinki. All private patient information was anonymized and de-identified prior to analysis.

Written informed consent was obtained from all participants for the use of their samples for scientific research and publication. Participants consented to (1) donation of blood or tissue samples, (2) provision of basic clinical information, and (3) exemption from the requirement for additional consent for future related research. These consent provisions were reviewed and approved by the IRB of Seoul National University Bundang Hospital and were confirmed to be exempt from further approval.

Study population

This study was conducted as part of a National Research Funding project under the BRIDGE Convergence R&D program of the Ministry of Science and ICT of the Republic of Korea, entitled “Development of Early Detection Technology for Pancreatic Cancer via Liquid Biopsy Using Fiber Optic-Based Raman Spectroscopy and Artificial Intelligence System” (Project number: NRF-2021M3C1C3097204).

A total of 150 human subjects were enrolled at a single tertiary hospital and categorized into three groups: 50 healthy controls, 40 patients with early-stage (resectable) PDAC, and 60 patients with advanced-stage PDAC (locally advanced or metastatic). Peripheral blood samples and associated clinical information were collected prospectively following approval by the IRB of Seoul National University Bundang Hospital. The established database has been approved for use in multiple research publications focusing on different engineering-based measurement methodologies.

Baseline demographic and clinical characteristics, including age, sex, tumor location, and tumor size, are summarized in Supplementary Table 2. The healthy control group was propensity-matched to the cancer groups with respect to age and sex, resulting in no statistically significant differences in these variables across the three groups. Healthy controls were selected from a health-screening population and had no history of pancreatic cystic neoplasm, chronic pancreatitis, familial pancreatic cancer, or other high-risk conditions. Individuals with evidence of diabetes mellitus, defined as hemoglobin A1c (HbA1c) > 6.5%, were excluded.

Tumor location did not differ significantly between the resectable and advanced PDAC groups, with pancreatic head tumors accounting

for approximately 46% of cases. Tumor size was significantly larger in the advanced PDAC group (median, 3.8 cm) than in the resectable PDAC group (median, 2.2 cm). All participants were Far East Asians (South Koreans).

Consideration of sex and gender (SAGER compliance)

Sex of participants was determined based on self-report at the time of enrollment and recorded in the clinical database. Sex and age were explicitly considered in the study design through propensity matching between healthy controls and patients with PDAC in order to minimize demographic confounding.

Sex- or gender-specific analyses were not performed in this study. This decision was made because the primary objective of the study was to evaluate the overall diagnostic performance of the assay across clinically relevant disease stages rather than to investigate biological or diagnostic differences between sexes. In addition, the available sample size was not powered to detect statistically meaningful sex-specific effects. Nevertheless, sex-disaggregated demographic data are provided in Supplementary Table 2, and individual-level sex information is included in the Source data files where applicable.

Participant compensation

No financial compensation was provided to participants for the donation or use of their biological samples.

Materials

Tetraethylorthosilicate (TEOS), (3-aminopropyl)triethoxysilane (APTES), gold (III) chloride trihydrate (HAuCl₄·3H₂O, 99.9%), sodium borohydride (NaBH₄), ascorbic acid, 1-ethyl-3-(3-dimethylaminopropyl)carbodiimide hydrochloride (EDC-HCl), N-hydroxysulfosuccinimide (sulfo-NHS), bovine serum albumin (BSA), 11-mercaptopundecanoic acid (11-MUA), 4-morpholineethanesulfonic acid (MES), AuNPs (20 nm diameter, 1 OD, stabilized suspension in citrate buffer), 96-well plate, and polyvinylpyrrolidone (PVP; Mw ~40,000) were purchased from Sigma-Aldrich (St. Louis, MO, USA). Hydrochloric acid (HCl; 35–37%), ethanol (99%), potassium hydroxide (KOH), and buffer solution (pH 9.0 ± 0.02) were purchased from Samchun Chemical (Seoul, Republic of Korea). Ammonium hydroxide (NH₄OH, 27%), sodium hydroxide (NaOH), and isopropyl alcohol (IPA) were purchased from Daejung (Busan, Republic of Korea). Phosphate-buffered saline (PBS; pH 7.4) and 0.5% (v/v) Tween 20 in PBS (PBST; pH 7.4) were purchased from Dyne Bio (Seongnam, Republic of Korea). Goat anti-mouse IgG antibody (Ab), backing card, NC membrane, and absorbent pads were purchased from Bore Da Biotech Co., Ltd. (Seongnam, Republic of Korea). An ELISA kit for CA19-9 (Cat# EHCA199) was purchased from Thermo Fisher Scientific (Waltham, MA, USA). CA19-9 monoclonal antibodies (A46300 and A46400) and CA19-9 antigen (J66100) were purchased from BiosPacific Inc. (Emeryville, CA, USA). Deionized water (D.W.) was used for all experiments.

Instruments and analysis

TEM images of the NPs were obtained using a JEM-F200 instrument (JEOL, Akishima, Tokyo, Japan) at a maximum accelerated voltage of

200 kV. Cs-STEM images of the NPs were obtained using a JEM-ARM200F(NEOARM) (JEOL, Akishima, Tokyo, Japan). The UV-vis-NIR extinction spectra of the NPs were obtained using an Optizen UV-vis spectrometer (Mecasys, Daejeon, Republic of Korea).

The solutions for the test and control lines were dispensed using an automated lateral flow reagent dispenser (Claremont Bio, Upland, CA, USA). The colorimetric signal intensities of the test line on the NC membrane were measured by using the ImageJ program. The colorimetric signal intensities of 96-microplate well after ELISA were measured by using BioTek Epoch 2 spectrophotometer (Agilent, Santa Clara, CA, USA).

Numerical simulations were performed using COMSOL Multiphysics 5.4. Calibration curves for CA19-9 were obtained using OriginPro 8.5. The ROC curve and AUC values of each analysis system were calculated using homemade R program code with the pROC library⁵⁷.

Numerical simulation of nanostructures

A wave optics simulation was performed to evaluate the optical behavior of the assembled nanostructure as a function of G_{Au} . TE-polarized electromagnetic waves in the wavelength range of 400–800 nm was applied. The wavelength dependence of the refractive index of Au was obtained from the database of Werner⁵⁸. Periodic conditions in the x- and y-directions and ports in the z-direction were applied for the backfield modeling. A perfectly matched layer in the x-, y-, and z-directions was set for scattered-field modeling.

To build an assembled nanostructure with evenly distributed AuNPs, we placed an AuNP in contact with the SiO₂ NP and rotated it to a specific angle to form similar gaps, as observed in the experiment.

Fabrication of SiO₂ NPs

SiO₂ NPs of approximately 145 nm in diameter were fabricated using a modified Stöber method⁵². TEOS (1.5 mL) and NH₄OH (1.5 mL) were added to absolute ethanol (35 mL) while stirring at 50 °C and 700 rpm with a magnetic bar. After 2 h, the fabricated SiO₂ NPs were washed five times with ethanol via centrifugation at 8885 × g for 10 min. The concentration of SiO₂ NPs was adjusted to 50 mg mL⁻¹ with absolute ethanol.

Amination of SiO₂ NPs (SiO₂-NH₂ NPs)

For the amination of SiO₂ NPs, 12.5 mg of SiO₂ NPs (in 250 μL of ethanol) was mixed with APTES (15.5 μL) and NH₄OH (10 μL). The mixture was shaken overnight, after which the SiO₂-NH₂ NPs were washed three times with ethanol via centrifugation at 6809 × g for 10 min. The concentration of the washed SiO₂-NH₂ NPs was adjusted to 10 mg mL⁻¹ with absolute ethanol.

Fabrication of Au nanoseeds

Prior to introduction, Au nanoseeds with diameters of 3–5 nm were prepared using the Martin method⁵⁹. Briefly, 5.67 mg of NaBH₄ in a 50 mM NaOH solution (3 mL) and 19.6 mg of HAuCl₄·3H₂O in a 50 mM HCl solution (1 mL) were sequentially added to 96 mL of D.W. while stirring at 1000 rpm. The color of the mixture changed to ruby-red after a short time, and the reaction continued for an additional 1 h. The prepared Au nanoseed mixture was stored at 4 °C for 2–3 days before use.

Fabrication of Au nanoseed-introduced SiO₂ NPs (SiO₂@Au NPs)

To fabricate the Au nanoseed-introduced SiO₂ NPs (SiO₂@Au NPs), Au nanoseeds (10 mL) and PVP (20 mg) were mixed. To this mixture, 2 mg of SiO₂-NH₂ NPs (in 200 μL of ethanol) was added, and the mixture was incubated overnight at room temperature. The fabricated SiO₂@Au NPs were washed three times with ethanol via centrifugation at 8885 × g for 10 min. The washed SiO₂@Au NPs were redispersed in 1 mL of 2% (w/v) PVP solution to adjust the concentration to 1 mg mL⁻¹.

Fabrication of AuNP-assembled SiO₂ NPs (SiO₂@Au@Au NPs)

To fabricate the SiO₂@Au@Au NPs, 0.2 mg of SiO₂@Au was added to 9.8 mL of 2% (w/v) PVP solution, and the mixture was stirred at 500 rpm. While stirring, 20 μL of a 10 mM HAuCl₄ solution and 40 μL of a 10 mM ascorbic acid solution were added to the mixture every 5 min, with the number of injections cycles varying as 1, 3, 5, 7, 9, and 11 times. The mixture was stirred for an additional 10 min after the final addition. The fabricated SiO₂@Au@Au NPs were washed five times with ethanol via centrifugation at 8885 × g for 10 min.

Removal of SiO₂ NPs from SiO₂@Au@Au_{II} NPs

First, 50 μg of SiO₂@Au@Au_{II} NPs was dispersed in 750 μL of IPA. Then, 250 μL of 4 M KOH was added, and the reaction was conducted for 24 h using an incubator mixer at 60 °C and 300 rpm. After the reaction was complete, the supernatant was removed by centrifugation at 27,237 × g for 15 min. The remaining AuNPs were sequentially washed twice with D.W. and 0.1% PBST (pH 7.4) via centrifugation at 27,237 × g for 15 min. The washed AuNPs were redispersed in 1 mL of 0.1% PBST (pH 7.4).

Conjugation of antibodies onto SiO₂@Au@Au_{II} NPs

Prior to the conjugation of antibodies, a carboxylic acid group was introduced by attaching 11-MUA onto SiO₂@Au@Au_{II} NPs. To achieve this, 0.1 mg of SiO₂@Au@Au_{II} NPs was redispersed in 90 μL of ethanol and mixed with 10 μL of a 2 mM 11-MUA solution. The mixture was shaken at room temperature for 1 h. After the reaction, the NPs were washed three times with ethanol via centrifugation at 8885 × g for 10 min. The surface-modified SiO₂@Au@Au NPs were then redispersed in 100 μL of ethanol.

Following the attachment of 11-MUA, the carboxylic acid group was activated. To activate the carboxylic acid group on the nanoparticles, a SiO₂@Au@Au_{II} NPs mixture (0.1 mg in 700 μL of D.W.) was sequentially mixed with 100 μL of a 2 mM EDC-HCl solution, a 2 mM sulfo-NHS solution, and a 500 mM MES solution. The reaction mixture was shaken for 30 min, after which the supernatant was removed by centrifugation at 9425 × g for 10 min. The remaining nanoparticles were redispersed in 1 mL of 50 mM MES individually, and then 10 μL of a CA19-9 monoclonal Ab (A46400) solution (1 mg mL⁻¹ in pH 7.4 PBS) was added to each mixture. The mixture was shaken at room temperature for 2 h.

The nanoparticles were washed twice with 50 mM MES via centrifugation at 9425 × g for 10 min and then redispersed in 1 mL of 50 mM MES after washing. After the reaction was complete, both nanoparticles were washed twice with 0.5% (v/v) PBST and 0.5% (w/v) BSA/PBS via centrifugation at 9425 × g for 10 min. The washed nanoparticles were stored at 4 °C prior to use.

Preparation of Ab-attached single AuNPs

Prior to the attachment of antibodies onto the surface of single AuNPs, 1 mL of AuNP solution (6.54 × 10¹¹ particles mL⁻¹, in citrate buffer) was removed via centrifugation, and the AuNPs were redispersed in 1 mL of buffer solution (pH 9.0). Then, 10 μL of CA19-9 monoclonal Ab (A46400) solution (1 mg mL⁻¹, pH 7.4 PBS) was added. The mixture was shaken at room temperature for 30 min and stored in a refrigerator at 4 °C for 24 h. Next, 100 μL of 10% (w/v) BSA/PBS was added to the mixture and shaken for 1 h. After the reaction was complete, the mixture was washed twice with PBS (pH 7.4) via centrifugation at 8885 × g for 10 min. The washed mixture was stored at 4 °C before use.

Preparation of test strips for CA19-9 detection

Test strips for SELFI and LFIA were prepared as follows. After assembling the NC membrane on the backing card, 1 mg mL⁻¹ of goat anti-mouse IgG Ab solution was dispensed onto the control line. Subsequently, an anti-CA19-9 capture Ab solution (1 mg mL⁻¹ in pH 7.4 PBS) was dispensed onto the test line. The distance between the control and

test lines was set at 4.0 mm. All solutions were dispensed onto the NC membrane at a flow rate of $1.9 \mu\text{L cm}^{-1}$. After dispensing, the NC membranes were dried in a desiccator for at least 2 h. After drying, the absorbent pad was attached to the backing card. The assembled strips were cut into 4 mm widths to fabricate individual test strips. This approach follows standard practices commonly used in LFIA fabrication²⁸.

Optimization of analysis time for SELFI

Prior to conducting SELFI analysis, the solvent of the $\text{SiO}_2\text{@Au@Au}_{11}$ NPs mixture was changed to 0.5% (v/v) PBST. A CA19-9 solution with a concentration of 370 U mL^{-1} in PBS (pH 7.4) was prepared. As a developing mixture, $33 \mu\text{L}$ of a mixture consisting of $3 \mu\text{L}$ of CA19-9 solution, $5 \mu\text{L}$ of $\text{SiO}_2\text{@Au@Au}_{11}$ NPs mixture, and $25 \mu\text{L}$ of 0.5% (v/v) PBST were mixed. The mixture was developed along each test strip for 1, 2, 5, 10, 15, 30, and 60 min. After development, the intensity of the colorimetric signal from the test strips was measured using the ImageJ software.

Model test for detection of CA19-9 with known concentrations

For SELFI and LFIA, the solvent of the $\text{SiO}_2\text{@Au@Au}_{11}$ NPs mixture and single AuNPs was changed to 0.5% (v/v) PBST. Subsequently, CA19-9 solutions of known concentrations ($0\text{--}200 \text{ U mL}^{-1}$) in PBS (pH 7.4) were prepared. Developing mixtures were prepared by mixing $3 \mu\text{L}$ of CA19-9 solution, $5 \mu\text{L}$ of $\text{SiO}_2\text{@Au@Au}_{11}$ NPs or single AuNPs mixture, and $25 \mu\text{L}$ of 0.5% (v/v) PBST. The developed mixture was allowed to flow along the test strips for 15 min. The intensities of the colorimetric signals from the test lines were measured using the ImageJ software after capturing photographs of the NC membranes. For ELISA, the signal intensities of the prepared CA19-9 sample solutions were measured using a BioTek Epoch 2 spectrophotometer.

Calibration curves for quantification of biomarkers using SELFI and LFIA

Prior to the quantitative analysis of CA19-9, the solvent of the $\text{SiO}_2\text{@Au@Au}_{11}$ NPs mixture and single AuNPs was changed to 0.5% (v/v) PBST. CA19-9 solutions with concentrations of 0, 0.0037, 0.037, 0.37, 3.7, 37, 370, 3700, and 37000 U mL^{-1} in pH 7.4 PBS were prepared. After preparing, developing mixtures by mixing $3 \mu\text{L}$ of CA19-9 solution, $5 \mu\text{L}$ of $\text{SiO}_2\text{@Au@Au}_{11}$ NPs or single AuNPs mixture, and $25 \mu\text{L}$ of 0.5% (v/v) PBST, the developing mixtures were allowed to flow along the test strips for 15 min. The intensities of the colorimetric signals from the test lines were measured using the ImageJ software, and the calibration curve was obtained by sigmoidal fitting. The general form of the sigmoidal-fitted (logistic model) calibration curve is as follows:

$$\text{Signal intensity} = A_2 + \frac{(A_1 - A_2)}{1 + \left(\frac{\text{Concentration}}{X_0}\right)^p} \quad (3)$$

where X_0 , A_1 , A_2 , and p are the calibration curve parameters. As next, Eq. (3) was rearranged in terms of concentration as follows:

$$\text{Concentration} = X_0 \times \left(\frac{A_1 - \text{Signal intensity}}{\text{Signal intensity} - A_2}\right)^{\frac{1}{p}} \quad (4)$$

Before calculating the LOD concentration using Eq. (4), the signal intensity at the LOD was calculated⁶⁰. Signal intensity at LOD (I_{LOD}) was calculated using the following equation:

$$I_{\text{LOD}} = I_{\text{Blank}} + 3 \times \sigma_{\text{Blank}} \quad (5)$$

where I_{Blank} is the signal intensity of the blank sample and σ_{Blank} is the standard deviation of the signal intensity in the blank sample. By

substituting the parameters and I_{LOD} for each case into Eq. (4), LOD of biomarker was calculated.

For PSA and ICAM-1 as target biomarkers, the entire process remained the same, except that the sample solution was substituted with PSA solutions (at concentrations of 0, 0.004, 0.04, 0.4, 4, 40, 400, 4000, and $40,000 \text{ ng mL}^{-1}$ in pH 7.4 PBS) or ICAM-1 solutions (at concentrations of 0, 0.002, 0.02, 0.2, 2, 20, 200, 2000, and 20000 ng mL^{-1} in pH 7.4 PBS).

Supplementary Table 1 presents the parameters for the calibration curves: I_{Blank} , σ_{Blank} , and LOD, for each case.

Quantification of CA19-9 in serum samples using ELISA

The concentration of CA19-9 in serum samples was measured using ELISA kits for CA19-9 according to the manufacturer's instructions. Serum samples were measured in duplicate, starting with a four-fold dilution and continuing up to a 200-fold dilution. CA19-9 concentrations were determined from standard curves of control proteins from the kits using a four-parameter logistic nonlinear regression model with a BioTek Epoch 2 spectrophotometer.

Quantification of CA19-9 in serum samples using SELFI and LFIA

Prior to the quantification of CA19-9 in the serum samples, the solvent of the nanoprobe mixture was changed to 0.5% (v/v) PBST. After that, $3 \mu\text{L}$ of serum samples, diluted 10-fold with 0.5% (v/v) PBST, were placed individually into a 96-well plate. The subsequent procedures were the same as those in the model test. The concentration of CA19-9 in each serum sample was calculated based on the signal intensity of the test lines and the calibration curves obtained in the model test.

Statistical analysis of quantified CA19-9 concentration using ELISA, LFIA, and SELFI

For the statistical analysis of quantified CA19-9 in the diagnosis of PDAC and comparison of each analytical system, an R program code incorporating the pROC library was designed and used⁵⁷. The total sample set consisted of three groups: 50 healthy controls, 40 patients with early-stage PDAC, and 60 patients with late-stage PDAC. To ensure robustness, 90% of the original samples (135 samples in this case) were selected by randomly excluding 10% of the samples from each group.

The ROC curves and AUC values were generated from these 135 samples, and this process was repeated 100 times to obtain 100 ROC curves and corresponding AUC values. The average ROC curves for ELISA and SELFI were determined using linear interpolation, whereas the ROC curve for LFIA was constructed using discrete decision thresholds derived from the minimum and maximum observed signal values. The average AUC values and 95% confidence interval (CI) ranges were calculated from the 100 AUC values obtained. This process remained consistent across all other cases, except for variations in sample group composition.

Statistics and reproducibility

No statistical method was used to predetermine sample size. Sample sizes were determined based on the availability of clinical specimens. All collected clinical samples were included in the quantitative analyses, and no data were excluded from the analyses. The experiments were not randomized. The investigators were not blinded to allocation during experiments and outcome assessment. Reproducibility was ensured through resampling-based statistical analyses, as described in the statistical analysis section. Random subsampling was performed using a fixed random seed, and model performance metrics were evaluated across repeated iterations.

Post hoc power analysis for sample size

Since this study leveraged all eligible cases recruited during the pre-defined enrollment period, a post hoc power analysis was performed

to assess whether the primary outcome measure was adequately powered. Based on the quantified results described above, the standardized effect size (Cohen's d), 95% CI, and statistical power were calculated using a custom R script incorporating the `cohen.d` and `pwr.t2n.test` functions from the `effsize` and `pwr` packages^{61,62} (Supplementary Table 3). All tests were two-sided with $\alpha = 0.05$.

Antibody use and validation

Antibodies used in this study and their applications are summarized here. Detector antibodies (anti-CA19-9; BiosPacific, Cat. No. A46400, anti-ICAM-1; Abcam, Cat. No. ab288641, and anti-PSA; Bore Da Biotech, Cat. No. 14801) were used for conjugation onto $\text{SiO}_2@Au@Au_{11}$ nanoprobe and single AuNPs at a concentration of 1 mg mL^{-1} . Capture antibodies (anti-CA19-9; BiosPacific, Cat. No. A46300, anti-ICAM-1; Abcam, Cat. No. ab288641, and anti-PSA; Bore Da Biotech, Cat. No. 14803) and goat anti-mouse IgG antibody (Bore Da Biotech, Cat. No. 20300) were used at 1 mg mL^{-1} as test line (capture antibodies) or control line (goat anti-mouse IgG antibody) reagents for LFIA test strips. An ELISA kit for CA19-9 (Thermo Fisher Scientific, Cat. No. EHCA199) was used according to the manufacturer's protocol, including all antibody concentrations and incubation conditions provided in the kit. Antibodies for ICAM-1 (Abcam, Cat. No. ab288641), supplied as a matched capture-detector pair, have been discontinued. All primary antibodies were validated by the manufacturers for human antigen detection in ELISA or sandwich immunoassays, as indicated in the respective datasheets.

Figure preparation

Figures 1a–c and 2f were created by the authors using Cinema 4D and Adobe Photoshop. Figure 2b was generated using COMSOL multiphysics and assembled for figure presentation. Figure 3a was assembled using Clip Studio Paint and Microsoft PowerPoint. Figure 4a was created using Microsoft PowerPoint. Supplementary Figs. 1 and 3c were rendered in Blender 4.2 LTS based on geometries generated using COMSOL Multiphysics. Supplementary Fig. 7 was created using Rhino 8, Cinema 4D, and Adobe Photoshop. Supplementary Fig. 11 was created using Cinema 4D.

Reporting summary

Further information on research design is available in the Nature Portfolio Reporting Summary linked to this article.

Data availability

The processed quantitative data generated in this study, including assay readouts and data used for statistical and ROC analyses, are provided in the Supplementary Tables associated with this paper. Individual-level clinical data derived from human serum samples are not publicly available due to ethical and legal restrictions related to participant privacy and the terms of informed consent. These data are stored in controlled-access repositories at the Human Bioresource Center of Seoul National University Bundang Hospital. Access to the restricted clinical data may be granted to qualified researchers for non-commercial research purposes, subject to approval by the Human Bioresource Center and the relevant Institutional Review Board. Requests for access should be directed to the corresponding author (Jong-chan Lee; ljc0316@snuh.org), who will coordinate the application process. A response to access requests is typically provided within 2–4 weeks. Data will remain available for the duration permitted by institutional and ethical regulations. Source data for all figures are provided with this paper. Source data are provided with this paper.

Code availability

The code used in this study is available at GitHub (<https://github.com/JKim-45/SELF1>) and has been archived on Zenodo with a <https://doi.org/10.5281/zenodo.17958691>.

References

- Siegel, R. L., Miller, K. D., Wagle, N. S. & Jemal, A. Cancer statistics, 2023. *CA Cancer J. Clin.* **73**, 17–48 (2023).
- Mizrahi, J. D., Surana, R., Valle, J. W. & Shroff, R. T. Pancreatic cancer. *Lancet* **395**, 2008–2020 (2020).
- Rawla, P., Sunkara, T. & Gaduputi, V. Epidemiology of pancreatic cancer: global trends, etiology and risk factors. *World J. Oncol.* **10**, 10–27 (2019).
- Rahib, L. et al. Projecting cancer incidence and deaths to 2030: the unexpected burden of thyroid, liver, and pancreas cancers in the United States. *Cancer Res.* **74**, 2913–2921 (2014).
- Kleeff, J. et al. Pancreatic cancer. *Nat. Rev. Dis. Primers* **2**, 16022 (2016).
- Eissa, M. A. L. et al. Promoter methylation of ADAMTS1 and BNC1 as potential biomarkers for early detection of pancreatic cancer in blood. *Clin. Epigenetics* **11**, 59 (2019).
- Kobi, M. et al. Imaging and management of pancreatic cancer. *Semin. Ultrasound CT MR* **41**, 139–151 (2020).
- Locker, G. Y. et al. ASCO 2006 update of recommendations for the use of tumor markers in gastrointestinal cancer. *J. Clin. Oncol.* **24**, 5313–5327 (2006).
- Ballehaninna, U. K. & Chamberlain, R. S. The clinical utility of serum CA 19-9 in the diagnosis, prognosis and management of pancreatic adenocarcinoma: an evidence based appraisal. *J. Gastrointest. Oncol.* **3**, 105–119 (2012).
- McGuigan, A. et al. Pancreatic cancer: a review of clinical diagnosis, epidemiology, treatment and outcomes. *World J. Gastroenterol.* **24**, 4846–4861 (2018).
- Blackford, A. L. et al. Pancreatic cancer surveillance and survival of high-risk individuals. *JAMA Oncol.* **10**, 1087–1096 (2024).
- Cohen, J. D. et al. Detection and localization of surgically resectable cancers with a multi-analyte blood test. *Science* **359**, 926–930 (2018).
- Pereira, S. P. et al. Early detection of pancreatic cancer. *Lancet Gastroenterol. Hepatol.* **5**, 698–710 (2020).
- Su, C.-W., Tian, J.-H., Ye, J.-J., Chang, H.-W. & Tsai, Y.-C. Construction of a label-free electrochemical immunosensor based on Zn-Co-S/graphene nanocomposites for carbohydrate antigen 19-9 detection. *Nanomaterials* **11**, 1475 (2021).
- Wu, S. et al. Collard-like $\text{Bi}_2\text{S}_3@Au$ nanocomposites-based label free electrochemical immunosensor for quantitative detection of CA19-9. *Talanta* **285**, 127299 (2025).
- Zhao, T. & Jin, B. A label-free electrochemical biosensor based on a bimetallic organic framework for the detection of carbohydrate antigen 19-9. *Anal. Methods* **16**, 6173–6182 (2024).
- Han, X., Lin, S., Li, Y., Cheng, C. & Han, X. Near-infrared photo-thermal immunoassay for pancreatic cancer biomarker CA 19-9 on a digital thermometer. *Anal. Chim. Acta* **1098**, 117–124 (2020).
- Xia, J., Li, Y., Xin, Y., Kang, L. & Lu, D. Early detection for carbohydrate antigen-19-9 based on surface enhanced Raman spectroscopy aptamer sensor. *Microchem. J.* **207**, 111750 (2024).
- Hwang, I.-J. et al. Confined growth of Ag nanogap shells emitting stable Raman label signals for SERS liquid biopsy of pancreatic cancer. *Biosens. Bioelectron.* **248**, 115948 (2024).
- Di Nardo, F., Chiarello, M., Cavalera, S., Baggiani, C. & Anfossi, L. Ten years of lateral flow immunoassay technique applications: trends, challenges and future perspectives. *Sensors* **21**, 5185 (2021).
- Wang, Z. et al. An overview for the nanoparticles-based quantitative lateral flow assay. *Small Methods* **6**, 2101143 (2022).
- Wang, J. et al. Hollow Au-Ag nanoparticles labeled immunochromatography strip for highly sensitive detection of clenbuterol. *Sci. Rep.* **7**, 41419 (2017).
- Wei, Z., Xi, Z., Vlasov, S., Ayala, J. & Xia, X. Nanocrystals of platinum-group metals as peroxidase mimics for in vitro diagnostics. *Chem. Commun.* **56**, 14962–14975 (2020).

24. Wei, Z., Luciano, K. & Xia, X. Catalytic gold-iridium nanoparticles as labels for sensitive colorimetric lateral flow assay. *ACS Nano* **16**, 21609–21617 (2022).
25. Kim, H.-M. et al. Au–Ag assembled on silica nanoprobe for visual semi-quantitative detection of prostate-specific antigen. *J. Nanobiotechnol.* **19**, 73 (2021).
26. Hong, D., Jo, E.-J., Jung, C. & Kim, M.-G. Absorption-modulated SiO₂@Au core–satellite nanoparticles for highly sensitive detection of SARS-CoV-2 nucleocapsid protein in lateral flow immunoassays. *ACS Appl. Mater. Interfaces* **14**, 45189–45200 (2022).
27. Kim, H.-M. et al. Multi-quantum dots-embedded silica-encapsulated nanoparticle-based lateral flow assay for highly sensitive exosome detection. *Nanomaterials* **11**, 768 (2021).
28. Bock, S. et al. Lateral flow immunoassay with quantum-dot-embedded silica nanoparticles for prostate-specific antigen detection. *Nanomaterials* **12**, 33 (2022).
29. Khelifa, L., Hu, Y., Jiang, N. & Yetisen, A. K. Lateral flow assays for hormone detection. *Lab Chip* **22**, 2451–2475 (2022).
30. Mahmoudi, T., Shirdel, B., Mansoori, B. & Baradaran, B. Dual sensitivity enhancement in gold nanoparticle-based lateral flow immunoassay for visual detection of carcinoembryonic antigen. *Anal. Sci. Adv.* **1**, 161–172 (2020).
31. Zhu, J. et al. One-pot synthesized Au@Pt nanostars-based lateral flow immunoassay for colorimetric and photothermal dual-mode detection of SARS-CoV-2 nucleocapsid antibody. *Anal. Chim. Acta* **1292**, 342241 (2024).
32. Huang, Y. et al. Lateral flow assay for carbohydrate antigen 19–9 in whole blood by using magnetized carbon nanotubes. *Microchim. Acta* **184**, 4287–4294 (2017).
33. Jiao, X. et al. Lateral flow immunoassay based on time-resolved fluorescence microspheres for rapid and quantitative screening CA199 in human serum. *Int. J. Mol. Sci.* **23**, 9991 (2022).
34. Shin, M. et al. Highly sensitive multiplexed colorimetric lateral flow immunoassay by plasmon-controlled metal–silica isoform nanocomposites: PINs. *Nano Converg.* **11**, 42 (2024).
35. Jain, P. K. & El-Sayed, M. A. Plasmonic coupling in noble metal nanostructures. *Chem. Phys. Lett.* **487**, 153–164 (2010).
36. Zuo, Z. et al. Multiple plasmon couplings in 3D hybrid Au-nanoparticles-decorated Ag nanocone arrays boosting highly sensitive surface enhanced Raman scattering. *Nano Res.* **15**, 317–325 (2022).
37. Su, D. et al. Ordered gold nanocluster-based plasmonic hotspot arrays for SERS detection of single molecules. *ACS Appl. Nano Mater.* **5**, 17067–17077 (2022).
38. Li, H., Merkl, P., Sommertune, J., Thersleff, T. & Sotiriou, G. A. SERS hotspot engineering by aerosol self-assembly of plasmonic Ag nanoaggregates with tunable interparticle distance. *Adv. Sci.* **9**, 2201133 (2022).
39. Li, X. et al. Au Multimer@MoS₂ hybrid structures for efficient photocatalytic hydrogen production via strongly plasmonic coupling effect. *Nano Energy* **30**, 549–558 (2016).
40. Yu, G. et al. Collective excitation of plasmon-coupled Au-nanochain boosts photocatalytic hydrogen evolution of semiconductor. *Nat. Commun.* **10**, 4912 (2019).
41. Ma, L. et al. Multi-interfacial plasmon coupling in multigap (Au/AgAu)@CdS core–shell hybrids for efficient photocatalytic hydrogen generation. *Nanoscale* **12**, 4383–4392 (2020).
42. Choi, I. et al. Colorimetric tracking of protein structural evolution based on the distance-dependent light scattering of embedded gold nanoparticles. *Chem. Commun.* **48**, 2286–2288 (2012).
43. An, H. J. et al. High-spatial and colourimetric imaging of histone modifications in single senescent cells using plasmonic nanoprobe. *Nat. Commun.* **12**, 5899 (2021).
44. Liu, D. et al. Ultrasensitive and stable Au dimer-based colorimetric sensors using the dynamically tunable gap-dependent plasmonic coupling optical properties. *Adv. Funct. Mater.* **28**, 1707392 (2018).
45. Materón, E. M. et al. Colorimetric detection of SARS-CoV-2 using plasmonic biosensors and smartphones. *ACS Appl. Mater. Interfaces* **14**, 54527–54538 (2022).
46. Kang, H. et al. Near-infrared SERS nanoprobe with plasmonic Au/Ag hollow-shell assemblies for in vivo multiplex detection. *Adv. Funct. Mater.* **23**, 3719–3727 (2013).
47. Choe, A. et al. Stretchable and wearable colorimetric patches based on thermoresponsive plasmonic microgels embedded in a hydrogel film. *NPG Asia Mater.* **10**, 912–922 (2018).
48. Sun, Z., Du, J., Duan, F., He, K. & Jing, C. Simulation and synthesis of Fe₃O₄–Au satellite nanostructures for optimised surface-enhanced Raman scattering. *J. Mater. Chem. C* **6**, 2252–2257 (2018).
49. De Silva Indrasekara, A. S. et al. Tailoring the core–satellite nanoassembly architectures by tuning internanoparticle electrostatic interactions. *Langmuir* **34**, 14617–14623 (2018).
50. Song, D. & Jing, D. Insight into the localized surface plasmon resonance property of core-satellite nanostructures: theoretical prediction and experimental validation. *J. Colloid Interface Sci.* **505**, 373–382 (2017).
51. Wang, Y. et al. Establishment of time-resolved fluorescence immunochromatographic assay for detection of carbohydrate antigen 19-9. *Sheng Wu Gong Cheng Xue Bao* **34**, 1012–1018 (2018).
52. Stöber, W., Fink, A. & Bohm, E. Controlled growth of monodisperse silica spheres in the micron size range. *J. Colloid Interface Sci.* **26**, 62–69 (1968).
53. Zhang, J. H., Zhan, P., Wang, Z. L., Zhang, W. Y. & Ming, N. B. Preparation of monodisperse silica particles with controllable size and shape. *J. Mater. Res.* **18**, 649–653 (2003).
54. Li, H. et al. Functionalized silica nanoparticles: classification, synthetic approaches and recent advances in adsorption applications. *Nanoscale* **13**, 15998–16016 (2021).
55. Ruan, Q., Shao, L., Shu, Y., Wang, J. & Wu, H. Growth of monodisperse gold nanospheres with diameters from 20 nm to 220 nm and their core/satellite nanostructures. *Adv. Opt. Mater.* **2**, 65–73 (2014).
56. Tempero, M. A. et al. Relationship of carbohydrate antigen 19-9 and Lewis antigens in pancreatic cancer. *Cancer Res.* **47**, 5501–5503 (1987).
57. Robin, X. et al. pROC: an open-source package for R and S+ to analyze and compare ROC curves. *BMC Bioinform.* **12**, 77 (2011).
58. Werner, W. S. M., Glantschnig, K. & Ambrosch-Draxl, C. Optical constants and inelastic electrons scattering data for 17 elemental metals. *J. Phys. Chem. Ref. Data* **38**, 1013–1092 (2009).
59. Martin, M. N., Basham, J. I., Chando, P. & Eah, S.-K. Charged gold nanoparticles in non-polar solvents: 10-min synthesis and 2D self-assembly. *Langmuir* **26**, 7410–7417 (2010).
60. Parolo, C. et al. Tutorial: design and fabrication of nanoparticle-based lateral-flow immunoassays. *Nat. Protoc.* **15**, 3788–3816 (2020).
61. Torchiano, M. effsize: Efficient Effect Size Computation (R package version 0.8.1). CRAN, <https://CRAN.R-project.org/package=effsize> (2020).
62. Champely, S., Ekstrom, C., Dalgaard, P., Gill, J., Weibelzahl, S. & Anandkumar, A. pwr: Basic Functions for Power Analysis. R package version 1.3-0. <https://CRAN.R-project.org/package=pwr> (2018).

Acknowledgements

This study was funded by the Ministry of Science and ICT (NRF-2022R1A2C2012883; B.-H.J.), the Bio and Medical Technology Development Program (2021M3C1C3097211; B.-H.J.), the National Research

Foundation of Korea (NRF) funded by the Korean government (MSIT) (RS-2023-00222910; J.-C.L. and B.-H.J., RS-2025-00558156; J.S.), and the National Institutes of Health (NIH) (R01DK133864; L.P.L.).

Author contributions

S.J., M.S., J.K., and B.-H.J. conceived and designed the experiments. S.J., M.S., J.H., H.-J.B., Y.Y., H.-S.C., K.Y., J.-S.C., J.A., G.A., and J.K. conducted experiments and analyses. J.K. developed custom R scripts for statistical analysis. S.J., M.S., J.H., Y.Y., J.K., J.-C.L., and B.-H.J. wrote the manuscript. S.J., M.S., J.H., H.C., J.-H.H., J.K., J.S., J.-C.L., L.P.L., and B.-H.J. revised the manuscript. L.P.L. and B.-H.J. supervised the overall process. All authors approved the final version of the manuscript. S.J., M.S., and J.H. contributed equally.

Competing interests

The authors declare no competing interests.

Additional information

Supplementary information The online version contains supplementary material available at <https://doi.org/10.1038/s41467-026-69204-7>.

Correspondence and requests for materials should be addressed to Jaehi Kim, Jihwan Song, Jong-chan Lee, Luke P. Lee or Bong-Hyun Jun.

Peer review information *Nature Communications* thanks Arben Merkoçi, Zhenpeng Qin and the other anonymous reviewer(s) for their

contribution to the peer review of this work. A peer review file is available.

Reprints and permissions information is available at <http://www.nature.com/reprints>

Publisher's note Springer Nature remains neutral with regard to jurisdictional claims in published maps and institutional affiliations.

Open Access This article is licensed under a Creative Commons Attribution-NonCommercial-NoDerivatives 4.0 International License, which permits any non-commercial use, sharing, distribution and reproduction in any medium or format, as long as you give appropriate credit to the original author(s) and the source, provide a link to the Creative Commons licence, and indicate if you modified the licensed material. You do not have permission under this licence to share adapted material derived from this article or parts of it. The images or other third party material in this article are included in the article's Creative Commons licence, unless indicated otherwise in a credit line to the material. If material is not included in the article's Creative Commons licence and your intended use is not permitted by statutory regulation or exceeds the permitted use, you will need to obtain permission directly from the copyright holder. To view a copy of this licence, visit <http://creativecommons.org/licenses/by-nc-nd/4.0/>.

© The Author(s) 2026